Spontaneous spin polarization and electron localization in constrained geometries: The Wigner transition in nanowires

D. Hughes and P. Ballone
Atomistic Simulation Centre, Queen's University Belfast, Belfast BT7 1NN, United Kingdom
(Received 30 March 2008; published 12 June 2008)

The Wigner transition in a jellium model of cylindrical nanowires has been investigated by density-functional computations using the local spin-density approximation. A wide range of background densities ρ_b has been explored from the nearly ideal metallic regime ($r_s=[3/4\pi\rho_b]^{1/3}=1$) to the high correlation limit ($r_s=100$). Computations have been performed using an unconstrained plane wave expansion for the Kohn–Sham orbitals and a large simulation cell with up to 480 electrons. The electron and spin distributions retain the cylindrical symmetry of the Hamiltonian at high density, while electron localization and spin polarization arise nearly simultaneously in low-density wires ($r_s\sim 30$). At sufficiently low density ($r_s\geq 40$), the ground-state electron distribution is the superposition of well defined and nearly disjoint droplets, whose charge and spin densities integrate almost exactly to one electron and $1/2\mu_B$, respectively. Droplets are arranged on radial shells and define a distorted lattice whose structure is intermediate between bcc and fcc. Dislocations and grain boundaries are apparent in the droplets' configuration found by our simulations. Our computations aim at modeling the behavior of experimental low-carried density systems made of lightly doped semiconductor nanostructures or conducting polymers.

DOI: 10.1103/PhysRevB.77.245312 PACS number(s): 73.21.Hb, 71.10.Hf, 75.75.+a, 73.63.Nm

I. INTRODUCTION

Advances in nanofabrication techniques and rising expectations in nanotechnologies have greatly enhanced our interest in natural and artificial structures whose linear dimensions are in the nanometer range.[1] Conducting nanowires represent a particularly interesting case since they are a necessary component of any nanometric device, and their fabrication, characterization, and control are likely to represent the most relevant challenges to be faced before the widespread application of nanotechnologies in electronic devices becomes a reality.[2] From a theoretical point of view, the interest is increased by their combination of a finite cross section with an extended dimension that allows us to investigate the interplay of confinement effects and conductivity.[3,4]

Nanowires have been produced and characterized by several methods. The fabrication of metallic nanowires, in particular, has reached the ultimate limit of subnanometric cross sections,[5,6] while retaining a significant conductivity. Early experiments relied on the formation and breaking of metal bridges connecting thicker metal leads. The aspect ratio of these structures, defined as the ratio of wire length over its radius, is sometimes fairly low, setting them into an intermediate class in between homogeneous linear wires and inhomogeneous point contacts. Longer wires of atomic thin diameter are obtained by filling and/or intercalating nanotubes (for instance, carbon, BN, MgO, or Ga_2O_3 nanotubes) with metal atoms,[7] or using nanotubes as lithography masks to produce long metal wires.[8] The valence density of these systems is almost exclusively determined by the chemical identity of the metal atoms and cannot be significantly varied, thus excluding the possibility of exploring a wide combination of confinement and electron correlation. Carbon nanotubes themselves represent an important family of nanowires, whose electronic and transport properties can be varied by selecting their size and structure, by controlling doping, and by changing physical conditions.[9]

Up to now the most widely used, and possibly the most flexible method to fabricate nanowires, has been based on the artificial nanostructures' technology, which has provided in fact the first practical route to prepare nanowires.[10] Also in this case, selective doping, thermal excitations, and/or continuous optical pumping are used to create a population of mobile charge carriers whose number can be controlled and varied over a wide density range.[11] The electrostatic potential of a gating semiconducting substrate may provide an additional parameter to control the system properties. The electron states in high-quality samples are fairly extended, somewhat reducing the effect of lattice defects, of doping fluctuations, and of the atomic scale modulation due to the semiconductor structure.[12]

A third class of nanowires consists of conducting polymers.[13] Doping is usually needed to give rise to conductivity and metallic behavior, and also in this case it represents the most crucial step to ensure the reproducibility of the sample properties. These systems share with artificial semiconductor nanowires the advantage of high flexibility in the choice of the valence charge density. Moreover, because of their soft interchain interactions, their properties can sometimes be tuned by changing physical parameters such as pressure, in addition to varying chemical conditions (for instance, changing the *p*H or the oxygen partial pressure) of the surrounding medium, allowing a finer system control.

The theoretical and computational literature on nanowires is abundant and still expanding very quickly. For this reason we limit ourselves to a short enumeration of the major theoretical issues concerning nanowires, and a brief discussion of the methods and results directly related to our study. First of all, nanowires arguably represent the closest approximation to one-dimensional (1D) conductors, whose properties are qualitatively different from those of their three-dimensional (3D) counterparts[14,15] since 3D conductors are generally de-

scribed by the Fermi liquid formalism,[16] while the Luttinger picture[17] is expected to provide the most appropriate description for the 1D case. Experimental results, however, show that genuine Luttinger liquid features are fairly rare,[18] and up to now have been identified mainly in carbon nanotubes,[19] in exotic inorganic[20] and organic[21] conducting polymers, and possibly in inhomogeneous systems with channel-like constrictions joining two mesoscopic or macroscopic conductors.[22]

Most of the nanowires made by nanofabrication, instead, behave like normal Fermi systems, even though confinement affects their properties up to relatively large diameters, giving rise to new phenomena and opportunities for advanced applications. Theory, computations, and experimental investigations of nanowires have in fact revealed a variety of unusual features in their ground state electronic structure, concerning especially their response to low-frequency (conductivity) and high-frequency (optical properties) electromagnetic perturbations. Prominent among these phenomena is the observation of a localization transition[23–25] and, possibly, of a spontaneous spin polarization[26,27] recently reported in the literature, which provide the primary motivation for the present study.

We present the results of density functional computations for a jellium model of a metallic nanowire, restricting ourselves to the simplest geometry, representing a cylindrical nanowire, translationally invariant along the axial direction. We focus on wires whose diameter is nanometric, but still well above (by 1 or 2 orders of magnitude) the atomic size limit, i.e., in a range that corresponds to recent realization of nanowires by artificial semiconductor techniques. As discussed below, several subbands are populated in this size range, thus justifying the usage of ordinary density-functional (DF) approximations in our study. In what follows we refer to the active particles as *electrons*, even though the model can be adapted to different types of charge carriers by an appropriate choice of the particle effective mass, of the system dielectric constant, and of the sign of the carried charge ($\pm e$).

Our computations cover a wide range of densities, from values typical of the valence charge of simple metals such as Al or the alkali metals, down to very dilute electron systems. The high electron density computations allow us to compare our results to those of previous studies. Our interest, however, is focused on the low-density regime, where the reduced dimensionality and the strong correlation give rise to a sequence of transitions leading to a highly localized electron distribution, consisting of nearly disjoint charge droplets, each corresponding to one spin-polarized electron. The results allow us to investigate the interplay of the two length scales characterizing the system, i.e., the Fermi wavelength and the wire radius, and to highlight the role of disorder in the droplets' configuration.

The same model has been extensively used in the past to investigate metal nanowires (see, for instance, Refs. 4 and 28–30; additional references will be cited in what follows), but, despite its simplicity, it still retains reasons of interest and many unexplored features. A closely related model has been used, in particular, to investigate the Wigner transition in jellium nanowires,[31] which is also the main subject of the present study. To the best of our knowledge, however, previous studies (including Ref. 31) relied on symmetry restrictions for the electron density and/or on simplified DF approximations. Several other studies focused on the thin-wire limit, restricting the system to 1D (see, for instance, Ref. 32 and 33). Delocalization in the plane perpendicular to the wire axis is accounted for by a modification of the electron-electron interaction removing the Coulomb singularity at short range. The prescription for this modification is not uniquely determined, and therefore an additional approximation is introduced, which is likely to be valid in the limit of atomic-thin wires, but it is less justified for the mesoscopic range investigated here. On the other hand, we emphasize once again that our length and energy units need to be rescaled using the appropriate dielectric constant and effective mass before a comparison with experimental data could be made. The fully unrestricted computations described below provide a high resolution view of the system structure and electronic properties and point to features and behaviors that have been repeatedly observed in nanometric wires whose density approaches that of the Wigner crystal.

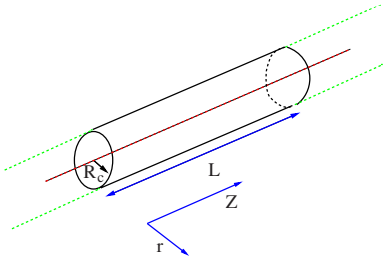

FIG. 1. (Color online) Schematic drawing of a cylindrical jellium nanowire.

II. MODEL AND COMPUTATIONAL METHOD

The model and the methods used in our investigation are closely related to general models and computational techniques widely used in condensed matter physics[34,35] and are briefly described here for completeness and in order to fix the notation. We consider a highly idealized model of nanowires consisting of a rodlike distribution of positive charge and of N electrons moving in the electrostatic field due to all the charges in the system. The wire segment has length L, is globally neutral, and is oriented along the z direction (see Fig. 1). Cylindrical coordinates (r,ϕ,z) are used throughout the paper, together with Hartree atomic units.

The simplest model is obtained by considering the following distribution of positive charge,

$$\rho_+(\mathbf{r}) = \rho_+(r,z) = \begin{cases} \rho_b & \text{for } r \le R_c, \quad 0 \le z < L \\ 0 & \text{for } r > R_c, \quad 0 \le z < L. \end{cases} \tag{1}$$

where R_c is the radius of the cylindrical charge density, and, in what follows, $R_c \ll L$. In other words, the positive density is constant and equal to ρ_b within the cylinder, and it vanishes outside. Following the standard practice of electron gas studies,[34] the background density ρ_b is measured by the radius r_s of the sphere that contains one unit charge ($r_s = [3/4\pi\rho_b]^{1/3}$).

The ground-state energy and electron density are computed by minimizing the functional of the electron density,

$$E_{\mathrm{KS}}[\{\psi_i\};i=1,\ldots,N]=\sum_{i=1}^{N}\langle\psi_i|-\frac{1}{2}\nabla^2+\frac{1}{2}V_{\mathrm{Ha}}(\mathbf{r})+u_{\mathrm{XC}}[\rho]|\psi_i\rangle \quad (2)$$

with respect to the N occupied Kohn–Sham (KS) orbitals $\{\psi_i\}$, which, in turn, determine the electron density according to the relation

$$\rho(\mathbf{r})=\sum_{i=1}^{N}|\psi_i(\mathbf{r})|^2. \quad (3)$$

Here V_{Ha} is the electrostatic potential of positive and negative charges, and therefore it includes the contribution of the *external* field due to the positive background as well as the Hartree potential due to the electron distribution. Moreover, $u_{\mathrm{XC}}[\rho]$ is the exchange-correlation (XC) energy per electron, which in our computations is given by the local spin-density (LSD) approximation.[36]

Quantum Monte Carlo (QMC) computations for spherical dots modeled by the same jellium approximation[37] have shown that in the case of finite metal systems represented by their valence charge only the LSD approximation provides results that are better than those of popular gradient corrected (GC) schemes,[38] which, on the other hand, provide a more accurate description of highly inhomogeneous systems such as (all-electron) atoms. Nevertheless, the application of LSD to low-density highly correlated states remains a severe approximation. Previous studies of the homogeneous electron gas (heg) phase diagram using DF (Ref. 39) have shown that, at variance from QMC, LSD predicts a unique transition from the paramagnetic, homogeneous fluid to a partially polarized nonuniform state, taking place at $r_s=22$. Such a density corresponds well to the magnetic transition as given by QMC (Ref. 40) but greatly overestimates the QMC value of the transition density to a bcc Wigner lattice.[41] However, LSD provides a fairly accurate description of the low-density localized phase, and its prediction of the energy ordering of different structures and spin configurations for the Wigner crystal agrees with the results of QMC computations. Therefore, we resort to LSD with the Perdew–Zunger form of the exchange-correlation energy[42] as a simple and prototypical model able to provide an approximate but still consistent description of the phase changes taking place in conducting nanowires. The quantitative details of the phase diagram, however, might need an *a posteriori* adjustment using the results of higher-order methods (such as QMC) not yet widely available.[43] It is interesting to remark that GC schemes such as the Perdew-Burke-Ernzerhof (PBE) approximation (Ref. 38) stabilize even further spin-polarized and space-localized configurations, thus moving the LSD estimate of the transitions points to even higher density.

The minimization of the functional (2) is equivalent to the self-consistent solution of the Schrödinger-type equations,

$$\left\{-\frac{1}{2}\nabla^2+V_{\mathrm{Ha}}(\mathbf{r})+\mu_{\mathrm{XC}}[\rho]\right\}|\psi_i\rangle=\epsilon_i|\psi_i\rangle \quad (4)$$

for the N states of lowest eigenvalues. In the equation above, $\mu_{\mathrm{XC}}[\rho]=u_{\mathrm{XC}}[\rho]+\rho du_{\mathrm{XC}}[\rho]/d\rho$ is the exchange-correlation potential corresponding to the exchange-correlation energy $u_{\mathrm{XC}}[\rho]$ of Eq. (2).

Finite-size effects are minimized by periodically repeating the basic segment in the z direction, thus approaching the limit of a geometric wire extending to infinity along a single direction. The periodicity along z implicitly defines a 1D Brillouin zone (BZ) of width $2\pi/L$, and electron states can be labeled with a continuous wave vector k_z belonging to the BZ. Results do not depend on the choice of the periodicity L and of the corresponding number N of electrons in the simulation cell for systems whose density is translationally invariant along z.

The cylindrical symmetry[44] of the external potential is retained by the electron density at least for r_s in the $2\leq r_s\leq 6$ range appropriate for the valence charge of simple metals. In such a case, Eq. (4) can be solved by separation of variables. First of all, the KS orbitals are factorized according to

$$\psi_{k_z}(\mathbf{r})=\chi(r)e^{im\phi}e^{i(2\pi/Ll+k_z)z}, \quad (5)$$

where m and l are relative integers and, following widely accepted conventions, k_z is selected in the interval $-(\pi/L)\leq k_z<(\pi/L)$.

The radial function $\chi(r)$ is then determined by solving the differential equation,

$$\frac{d^2\chi(r)}{dr^2}+\frac{1}{r}\frac{d\chi(r)}{dr}+\left[2(\epsilon-V_{\mathrm{KS}}(\mathbf{r}))-\left(\frac{2\pi l}{L}+k_z\right)^2-\frac{m^2}{r^2}\right]\chi(r)=0, \quad (6)$$

subject to the appropriate boundary conditions that for bound states read

$$\lim_{r\to 0}\chi(r)=r^m(a_0+a_1r+a_2r^2), \quad (7)$$

$$\lim_{r\to\infty}\chi(r)=\frac{\exp(-\sqrt{-\epsilon}r)}{\sqrt{r}}. \quad (8)$$

These conditions can be satisfied for a discrete set of negative eigenvalues, which we indicate with $\epsilon_{nm}(k_z+\frac{2\pi l}{L})$, where n is a positive integer analogous to the principal quantum number of atoms. The corresponding radial functions $\chi(r)$ depend on the n and m quantum numbers, while they are independent of l and k_z, and in what follows they will be denoted by $\chi_{nm}(r)$. In addition to these bound states, the system has a continuum of scattering states whose eigenvalues are positive. The ground-state density is given by

$$\rho(r) = \sum_{nml} \int_{BZ} f\left[\epsilon_{nm}\left(k_z + \frac{2\pi l}{L}\right)\right] |\chi_{nm}(\mathbf{r})|^2 dk_z, \tag{9}$$

where $f[\epsilon]$ is the occupation number. In the case of a cylindrical ground state, the z-momentum dependence of $\epsilon_{nm}(k_z)$ is given by

$$\epsilon_{nm}(k_z) = \epsilon_{nm}(k_z = 0) + \frac{k_z^2}{2}, \tag{10}$$

and the integration over k_z can be performed analytically.[29] States are occupied up to an energy ϵ_F such that the number of states whose energy is less than ϵ_F is equal to the number of electrons in the system. The total number of distinct $\{nm\}$ combinations found for the occupied states is by definition the number of occupied subbands for the wire under investigation. As detailed below, this number is of the order of 10 for the sizes investigated in our study.

In our computation a radial grid of 2000 points has been used, extending up to $R_{\max}=4R_c$ in the case of high-density samples ($r_s<10$) and up to $R_{\max}=2R_c$ for low-density systems. Each orbitals is integrated outward from $r=0$ and inward from $R_{\max}$ using a predictor-corrector method. The corresponding eigenvalue is determined by the matching of the two solutions at R_c. Angular momenta up to $m=20$ have been considered, and degenerate levels are equally populated at all stages of the calculation. A similar computational procedure is adopted for the determination of the Coulomb potential from the charge density.

Apart from the k_z label and apart from obvious differences in the radial equations, the approach is completely analogous to methods routinely used to compute the electronic structure of atoms with the restriction to spherical symmetry, and high accuracy solutions can be obtained relatively easily with a limited computational effort. The method outlined above has been used several times to determine the ground-state properties of jellium wires whose density has cylindrical symmetry.[4,28] It has been implemented one more time by us, and the solutions have been used to test the accuracy and convergence of the results provided by a more general but computationally more intensive method.

The restriction to cylindrical symmetry for the electron density has to be abandoned in order to describe broken symmetry solutions, expected to arise at low ρ_b densities, and also in the case of wires subject to an external perturbation not conserving the original symmetry. In those cases a general solution is obtained upon expanding KS orbitals in plane waves,

$$\psi_{\mathbf{k}}^{(i)}(\mathbf{r}) = \sum_{\mathbf{G}} c_{\mathbf{G}}^{(i)} e^{i\mathbf{G}r} e^{i\mathbf{k}r}. \tag{11}$$

In doing so we assume that the system is periodic in 3D, and we impose a fictitious periodicity of length (L_x, L_y) in the plane perpendicular to the z axis. Among other things, this periodicity implies that the label $\mathbf{k}$ is now a 3D vector. The plane wave expansion of Eq. (11) is limited to those $\mathbf{G}$ vectors such that $|\mathbf{G}+\mathbf{k}|^2$ is less than a preselected cutoff E_{cut}, which has the dimensions of an energy, and in what follows is measured in Rydbergs.

The functional $E_{\text{KS}}[\{\psi_i\}]$ is in fact is a function of the multitude of $\{c_{\mathbf{G},k}^{(i)}\}$ coefficients, and it can be optimized by iterative minimization using the information provided by the gradient,

$$\begin{aligned}\frac{\partial E_{\text{KS}}}{\partial c_{\mathbf{G},k}^{(i)}} &= \sum_{\mathbf{k}} \int \frac{\delta E_{\text{KS}}}{\delta \psi_{\mathbf{k}}^{(i)}(\mathbf{r})} \frac{d\psi_{\mathbf{k}}^{(i)}(\mathbf{r})}{dc_{\mathbf{G}}^{(i)}} d\mathbf{r} \\ &= \sum_{\mathbf{k}} \int \frac{\delta E_{\text{KS}}}{\delta \psi_{\mathbf{k}}^{(i)}(\mathbf{r})} e^{i\mathbf{G}r} d\mathbf{r} \\ &= \sum_{\mathbf{k}} \int H_{\text{KS}}[\rho, \mathbf{k}] \psi_{\mathbf{k}}^{(i)}(\mathbf{r}) e^{i\mathbf{G}r} d\mathbf{r}. \end{aligned} \tag{12}$$

The sum over $\mathbf{k}$ points is a discretized version of the integral over the Brillouin zone implied by the 3D periodicity.

The actual optimization may be achieved by a variety of methods,[45] including steepest descent, conjugate gradient, etc. We used a simple interpolation-minimization scheme that will be described elsewhere. In all cases the energy minimization is performed at fixed spin polarization $\zeta=(n_+ - n_-)/(n_+ + n_-)$, where n_+ and n_- are the spin-up and spin-down charges, respectively. The sum of n_+ and n_- is equal to N, although neither of the two partial charges needs to be an integer if the system is a metal. The empty states are determined by minimizing the sum of their KS eigenvalues in the fixed potential of the ground state density.

The iterative approach briefly outlined in this section closely follows the plane wave methods developed for *ab initio* simulations, and a variety of technical details can be found in Ref. 45. The approach and the related computer program can be easily adapted to account for more realistic pseudopotential models and to allow the simultaneous motion of ionic and electronic degrees of freedom whenever the shape of the positive charge is allowed to evolve in time.

As described below, for low r_s (high density) and up to at least $r_s=20$, the ground-state density turns out to be cylindrically symmetric, and the cutoff energy for the 3D-plane wave computation is tuned by the comparison with the results of the radial program using full cylindrical symmetry. Total energies computed by the two methods shows that convergence in the plane-wave expansion is already achieved at a cutoff energy of $E_{\text{cut}}(r_s) \sim 10/r_s^2$ Ry. The localized states found at low density ($r_s \geq 30$) are more difficult to represent in plane waves, and explicit tests have shown that a cutoff energy of $E_{\text{cut}}=20/r_s^2$ Ry is required for a uniform convergence of ground-state properties over the full density range $1 \leq r_s \leq 100$ explored in our study. More details on convergence are given below, in relation to the precise conditions (size, density, and net spin polarization) of our computations. Despite the relatively low cutoff, the large cell size implies that the number of variational degrees of freedom is of the order of 5×10^4 *per state*. Taking into account the high number of states included in our computations, it is not surprising to find that the minimization of the energy functional turns out to be relatively time consuming, requiring ~ 10 days on a single AMD Opteron (2.2 GHz) processor even for the smallest ($N=240$) system size.

We emphasize that while the nominal (or net) spin polarization $\zeta=(N_+-N_-)/(N_++N_-)$ is an input parameter of our computations, the spin density $\rho_S(\mathbf{r})=\rho_+(\mathbf{r})-\rho_-(\mathbf{r})$ is fully unconstrained both in the radial cylindrical and in the plane wave approach, and $I_S=\int|\rho_S(\mathbf{r})|d\mathbf{r}$ can be significantly larger than $|N_+-N_-|$. In particular, at low background density ($r_s>30$) local spin polarization is found also in nominally paramagnetic samples at $\zeta=0$.

III. COMPUTATIONAL RESULTS

Computations have been performed for a series of wires of length $L=32r_s$ periodically repeated along z, consisting of $N=240$ electrons moving in the electrostatic potential of a cylindrical distribution of positive charge whose plasma parameter r_s spans the range $1\leq r_s\leq 100$. At $r_s=1$, therefore, the radius of the positive charge is $R_c=3.162$ a.u., or 1.673 Å, and the wire segment explicitly included in the computation is 16.93 Å long. The radius reaches 167.3 Å at the lower-density range ($r_s=100$), and in such a case the periodicity along z is 1693 Å or 0.1693 μm. All wires have the same aspect ratio $L/R_c=10.12$.

Plane-wave computations have been performed using a cubic simulation box of side L, and, therefore, the background density occupies ~3% of the simulation box. We verified that the overlap of KS orbitals and electron densities from periodic replicas of the central wire is negligible. In order to investigate the size dependence of the results, plane-wave computations have been performed also for larger systems ($N=480$ electrons) and $r_s=1$, 20, 30, 40, and 70. The same simulation box of the $N=240$ samples has been used for this second set of computations, and the aspect ratio of the wires turns out to be $L/R_c=7.2$.

Because of the fairly large size of our samples and considering also their low average density, the sampling of the system Brillouin zone in the plane-wave computations has been restricted to the Γ-point only. The electron density of states (DOS) resulting from the Γ-point sampling reproduces only qualitatively the exact result (see Fig. 2 for the $N=240$ electrons system at $r_s=20$). However, test computations for different system sizes and/or better k_z sampling show that the discretization of the DOS does not affect the results in a significant way, and, in particular, it changes only slightly the relative stability of different phases in the transition region. Moreover, the role of k_z points is decreased by the fact that the systems we are primarily interested in (i.e., the low electron-density wires) are in fact insulators.

The full range of spin polarizations $0\leq\zeta\leq 1$ has been explored by varying the relative number of spin-up (N_+) and spin-down (N_-) electrons, starting from the paramagnetic case ($N_+=N_-=120$), and progressively increasing (decreasing) N_+ (N_-) in steps of ten electrons up to $N_+=240$ ($N_-=0$). We use here N_+ and N_- instead of n_+ and n_- to indicate that the net spin imbalance $N_{\text{spin}}=N_+-N_-$ is restricted to integer values.

A. Computations in the radial-cylindrical approach

The results obtained by the radial code under the restriction of cylindrical symmetry are summarized in Figs. 3 and 4. Our data agree with those of previous computations[28,29] whenever a comparison is possible.

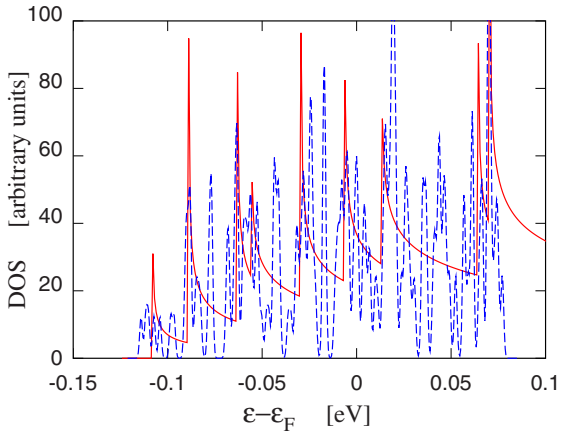

FIG. 2. (Color online) Comparison of the exact DOS (full line) with the approximate result from a Γ-point computation (dash line) for a 240-electron wire of length $L=32r_s$ and diameter $2R_c=6.326r_s$ at $r_s=20$. The electronic configuration (ground state) is paramagnetic. The discrete eigenvalues of the Γ-point computation have been convoluted with a Gaussian of 7.2510^{-4} eV half-width.

As pointed out in Ref. 29, the enhancement of the exchange interaction due to confinement, together with the degeneracies of cylindrical wave functions in very thin wires may give rise to a progressive filling of subbands reminiscent of Hund's rule in atoms. In turn, this implies that partial polarization may arise at densities as high as those of bulk sodium ($r_s=4$). The integral of the spin polarization density $\rho_S(\mathbf{r})=\rho_+(\mathbf{r})-\rho_-(\mathbf{r})$ is small, amounting to a few electrons at most, and, therefore, the relative spin polarization is fairly low as soon as the wire radius exceeds monatomic thickness. Moreover, as expected, $\rho_S(\mathbf{r})=\rho_+(\mathbf{r})-\rho_-(\mathbf{r})$ always peaks at the background edge in high-density samples, and spin polarization might indeed represent the precursor of spin polarized states quasilocalized at the surface of the semi-infinite jellium.

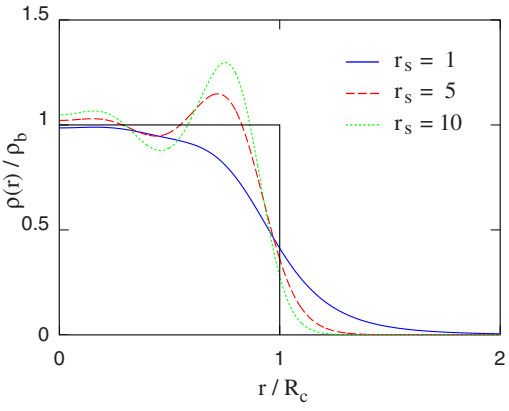

FIG. 3. (Color online) Electron density $\rho(r)$ as a function of the radial coordinate r at three values of the electron gas parameter r_s, computed using the 1D algorithm under the assumption of cylindrical symmetry (Ref. 44). The positive density distribution has radius $R_c=3.162r_s$, and the ground state is paramagnetic for the three cases displayed here.

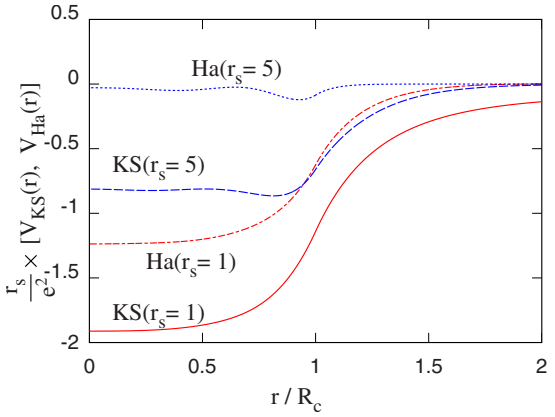

FIG. 4. (Color online) Radial dependence of the Kohn–Sham potential $V_{KS}(r)$ (full line) and of the electrostatic potential $V_{Ha}(r)$ for wires at $r_=1$ and $r_s=5$.

Extensive spin polarization in the ground state appears only at much lower density, far below those found in elemental metals, but achievable in artificial conductors obtained by doping semiconducting structures or polymeric chains. A plot of the spin polarization energy $\Delta E_S(\zeta)=E_{tot}(\zeta)-E_{tot}(0)$ for the wire and for the homogeneous electron gas shows that at low density and for the relatively thick wires considered in our study, the stabilization of the spin polarization brought about by confinement and by inhomogeneity is fairly modest (see Fig. 5). Nevertheless, computations in the cylindrical symmetry approximation show that the transition to a (partially) spin-polarized ground state takes place at $r_s=27$. At variance from what has been found in high-density wires, the spin polarization in low-density (nominal $\zeta\sim 0$) low-spin-polarization samples tends to be localized in the central region of the wire, with only negligible contributions from regions beyond the background radius.

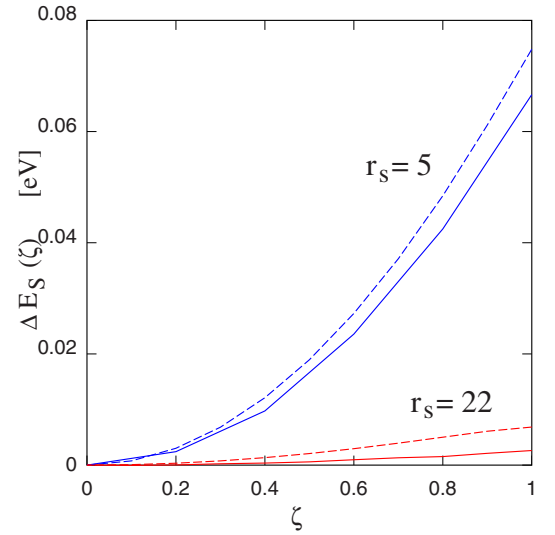

FIG. 5. (Color online) Spin polarization energy $\Delta E_S(\zeta)=E_{tot}(\zeta)-E_{tot}(0)$ for the wire (full line) and for the homogeneous electron gas (dash line). Computations have been performed for a finite system with $N=240$ electrons under the assumption of a cylindrically symmetric charge density.

A detailed comparison of the phase change observed in wires with the same paramagnetic to ferromagnetic transition in the heg is in order. In our computations we use the local-density exchange-correlation approximation of Perdew and Zunger[42] (PZ). Together with the elementary expression for the kinetic energy of plane wave KS orbitals,[46] the PZ approximation gives an expression for the polarization energy $\Delta E_S^{heg}(\zeta)$ of the heg, which has a minimum at $\zeta=0$ for $r_s\leq 75$ and at $\zeta=1$ for $r_s>75$. The magnetic transition in the heg as described by the PZ formula, therefore, is first order; it corresponds to the change from paramagnetic at high density to fully spin polarized at low density and takes place at $r_s=75$, i.e., at a density far below the one found in the wire computations. It is important to note, however, that plane wave computations for the extended electron gas using the same PZ approximation but without the homogeneity restriction for the electron density in the jellium model do find the transition at $r_s=22$.[39] In this case, the transition takes place between the paramagnetic homogeneous state stable at high density and a partially spin polarized inhomogeneous electron density at higher r_s. Our computations for wires using the radial-cylindrical formalism exclude density modulations along z, but partial spin polarization is allowed, as well as partial localization in the radial direction, manifesting itself in the enhancement of the density oscillations along the radial direction with increasing r_s. These two effects combined are responsible for the change of the transition point from $r_s=75$ in the heg to $r_s\sim 27$ in wires. We emphasize, however, that this displacement of the transition density is due far more to the release of the homogeneity constraint (along r) than to confinement and reduced dimensionality, even though these effects also play a secondary role, as will be shown below.

In the past, the discrepancy between the $r_s=75$ transition for the heg implicit in the PZ exchange-correlation interpolation and the results of plane wave computations has been attributed to a failure of LSD for highly correlated systems. However, it is difficult at present to unambiguously conclude whether this is indeed the case, or whether the LSD-plane-wave result faithfully predicts a real jellium property. In fact, despite a growing number of quantum MC studies,[36,40,41] the exploration of the jellium phase diagram is still incomplete, and, in particular, computations for partially spin polarized *and* partially localized states (see below the discussion of localization in the KS orbitals) similar to those found by LSD have never been carried out for densities corresponding to $r_s=30$.

B. Plane-wave computations

Electron localization is fully accounted for by the 3D-plane-wave computations, whose results display the same magnetic transition at nearly the same density of the radial-cylindrical computations. More precisely, up to $r_s=30$ the solutions found by the plane-wave code also display translational invariance along z at all ζ, and, apart from occasional interchanges of nearly degenerate states, the corresponding sequence of KS orbitals agrees with that of the radial computations for full cylindrical symmetry. As anticipated in Sec.

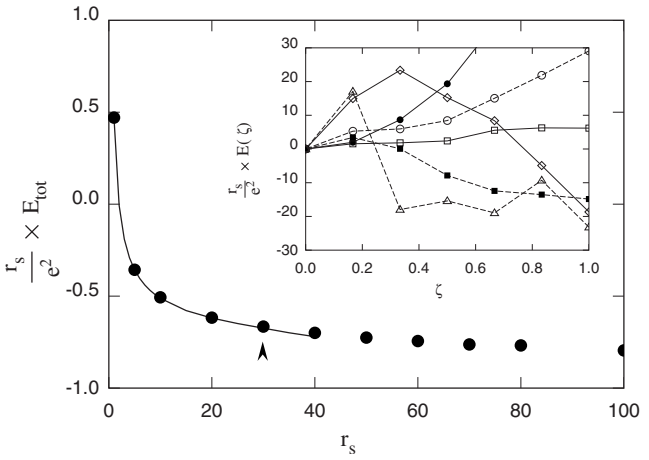

FIG. 6. Total energy per electron of jellium wires computed by the radial-cylindrical method (full line) and by the 3D-plane-wave method (full dots). At each r_s the energy of the lowest-energy spin configuration is reported. The arrow marks the transition between paramagnetic and partially spin-polarized configurations. The polarization energy per electron $\Delta E_S(\zeta)$ at six background densities is shown in the inset. Full dots, $r_s=1$; circles, $r_s=20$; squares, $r_s=30$; filled squares, $r_s=40$; diamonds, $r_s=70$; and triangles, $r_s=100$.

II, the convergence of the plane-wave expansion is confirmed by the good agreement of the total energy obtained by the two computational approaches (see Fig. 6).

Sizable differences between the solutions of the radial scheme and those of the plane-wave computation first appear at $r_s=30$. Inspection of the electron density found by the unconstrained plane wave minimization (see Fig. 7) reveals that an apparent localization transition involving all coordinates (i.e., now including z) takes place in the samples of highest spin polarization ($\zeta \geq 0.5$). Localization can be described as *partial* because the overlap of different electron density peaks is significant, and the density at local minima is still a sizable fraction of ρ_b (see the inset in Fig. 7). We verified that the density modulation along z remains nearly unchanged when the sampling of the BZ is extended to more k_z points. Further analysis described below suggests that the electron configuration consists of a majority of delocalized states similar to those found at high density, coexisting with localized states whose energy is at the bottom and at the top of the occupied (valence) band. We remark that up to $r_s=40$ localization in the radial direction, giving rise to a sequence of well defined electron-density shells, is more marked than localization within each of the radial shells. Moreover, localization is stronger in the inner region of the wire and somewhat attenuated in the outer electron shell, as apparent in Fig. 7.

Comparison of the different energy contributions for the z-invariant and for the localized states show that, as expected, localization is driven by a gain in correlation energy, only partly compensated by the kinetic energy term, which increases upon localization. This energy balance, in turn, explains why localization takes place at first in spin polarized samples since the kinetic energy[46] of ferromagnetic states is higher than that of the paramagnetic state, while their correlation energy is lower. On the other hand, the kinetic energy of the Wigner crystal is nearly independent of spin, and thus, the kinetic energy cost of localized states is less relevant for the ferromagnetic configuration, while the potential gain in correlation energy is comparatively larger. Both energy terms, therefore, point to high spin configurations as the first candidates for localization.

Despite the energy gain provided by localization, at $r_s=30$ the ferromagnetic configuration is still slightly higher in

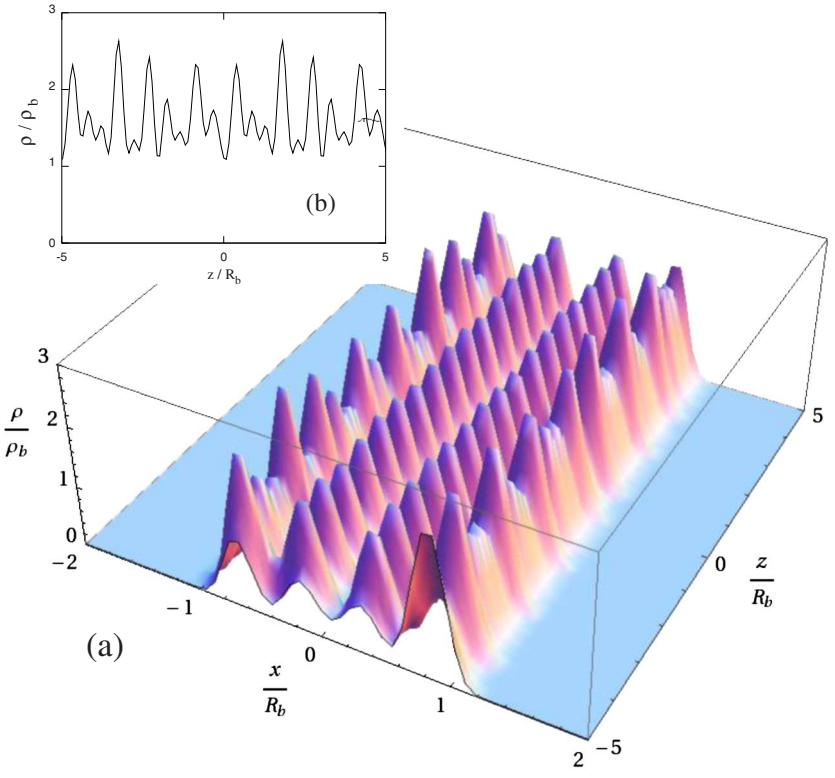

FIG. 7. (Color online) Electron density of a fully spin polarized jellium wire obtained by the plane wave method. $N=240$, $r_s=30$. Panel (a): 2D plot of the density $\rho(r,z)$ on the axial plane $\phi=0$. Panel (b): 1D plot of the electron density $\rho(z)$ along the line parallel to the cylindrical axis of coordinates: $x-a=y=0$, where $a=2.25 \times r_s=0.71R_c$

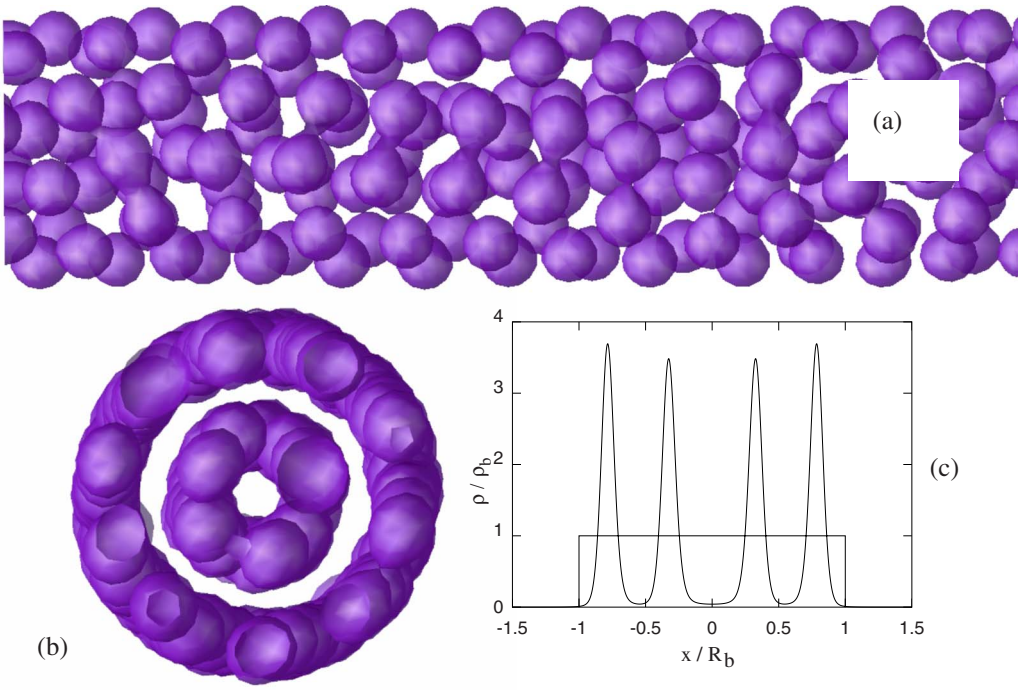

FIG. 8. (Color online) Electron-density contour plot for the ferromagnetic ground state of the $r_s=70$, $N=240$ wire. Panel (a): transversal view. Panel (b): perspective view. Panel (c): radial density profile obtained upon averaging the 3D density over ϕ and z.

energy than the paramagnetic z-invariant state. The energy difference between the two, however, is very small, and, in fact, the ground-state energy is almost constant over the entire $0 \leq \zeta \leq 1$ range, suggesting that in the vicinity of the localization transition spin glass features might arise from the near degeneracy of several different spin states. This same near degeneracy with respect to changes of ζ makes it difficult to provide an accurate determination of the net ground state spin polarization at densities close to the transition point (see the inset in Fig. 6). Nevertheless, plane-wave computations confirm the stability of partially polarized stated at r_s slightly higher than 30, as already anticipated by the radial-cylindrical computations. Of course, these observations imply that the transition to the spin polarized state is at most weakly first order.

The fully ferromagnetic state becomes the state of lowest energy for $r_s \geq 35$, the shift in the transition point from $r_s=27$ estimated in the radial cylindrical method due to the discretization of the DOS, and to the finite plane wave expansion of orbitals and electron density, which affects spin-polarized systems slightly more than the paramagnetic ones. In the low-density regime at $r_s \geq 40$, localization is apparent in all systems, irrespective of spin polarization, and becomes progressively more marked with increasing r_s. Plots of constant electron density surfaces (isosurfaces, in what follows) provide a direct and intuitive view of the localization extent in low-density systems, as apparent from Fig. 8 showing the $\rho=1.6\rho_b$ isosurface for the ferromagnetic ground state at $r_s=70$. Shell effects are apparent from the transversal view of the density distribution [Figs. 8(b) and 8(c)] and might be seen as the oversized and frozen-in version of the charge (Friedel) oscillations already present in the high density liquid phase (see Fig. 3). The perspective view of the same isosurface [Fig. 8(a)] clearly shows that the system consists of an assembly of well defined charge droplets. In what follows, these droplets will sometimes be referred to as *charge blobs* to account for their somewhat irregular shape.

The gradual organization of charge into shells with increasing r_s, followed by the breakdown of shells into one-electron droplets is qualitatively similar to the two-stage freezing (or, equivalently, melting) observed in 2D circular quantum dots (see, for instance, Ref. 47), whose radial and orientational orders set in at different densities and/or temperatures. Only for sufficiently large systems the two localization processes merge into a unique freezing transition.

The fairly regular pattern displayed by the droplets distribution in low-density samples suggests that a geometrical lattice, possibly closely related to the bcc structure of the extended Wigner crystal, might underlay the ground state charge configuration. To identify this ideal geometry, the continuous density distribution provided by LSD is mapped onto a particles configuration by (i) first identifying connected regions whose density is higher than $\rho_{\mathrm{cut}}=2\rho_b$, and then (ii) associating one particle to each of these domains, and locating it at the center of mass of the corresponding charge distribution. This procedure provides a fully unambiguous result only for systems of fairly high r_s ($r_s>50$). For these low-density systems, the number of connected regions (and thus the number of associated particles) is always very close to the number N of electrons in the system, the difference being at most a few units in all samples at $r_s \geq 70$, thus lending a reality flavor to the representation of the electron

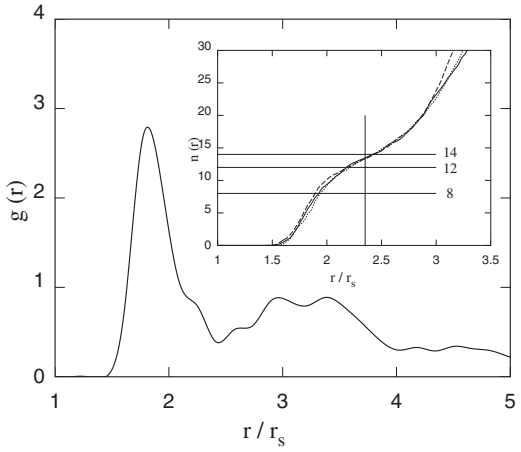

FIG. 9. Radial distribution function of particles representing charge blobs (see text) for a wire of $N=240$ electrons at $r_s=70$ and $\zeta=1$. Inset: running coordination number $n_c(r)$ of particles representing charge blobs. Full line: $N=240$ electrons, $r_s=70$, $\zeta=1$; dash line: $N=480$ electrons, $r_s=70$, $\zeta=1$; and dotted line: $N=240$ electrons, $r_s=100$, $\zeta=1$. The horizontal lines correspond to full shells of neighbors in the bcc ($n_c=8$ and $n_c=14$) and in the fcc ($n_c=12$) lattice. The vertical line corresponds to the minimum of $g(r)$ and defines the cutoff radius for the computation of the average coordination number.

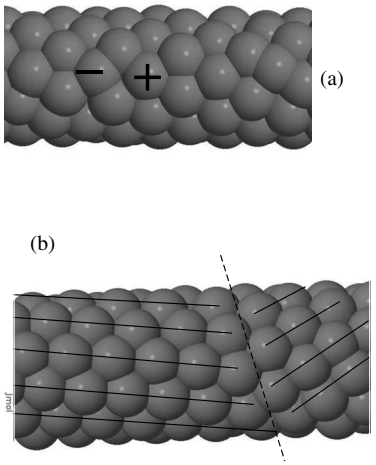

FIG. 10. Defective configurations in the ground-state distribution of charge droplets of fully spin-polarized wires at $r_s=70$: (a) pair (+,−) of miscoordinated droplets in the middle shell of the $N=480$ sample; (b) grain boundary on the inner shell of the $N=240$ sample.

density by particles. The configuration obtained in this way closely resembles the low temperature structure of classical particle models such as the one component plasma (OCP), as obtained by slowly annealing liquid samples. In this respect, it is interesting to note that the radial distribution function $g(r)$ of the representing particles[48] belonging to the inner radial shells of the computed structures displays the same characteristic features found in the glassy state of the classical one-component plasma,[49] consisting in an asymmetric first peak and a split second peak (see Fig. 9).

The radial distribution function of particles representing charge blobs depends only weakly on spin polarization (see below) and on density for $r_s \geq 70$, apart a trivial scaling of all distances. The dependence on sample size is also very weak up to the second peak of $g(r)$, while it becomes important at larger distances. These results are reflected in the weak density and size dependence of the running coordination number $n_c(r)$ defined as

$$n_c(r) = 4\pi\rho_b \int_0^r r'^2 g(r') dr' \tag{13}$$

and displayed in the inset of Fig. 9.

Despite the unambiguous mapping of charge blobs into particles, the identification of the ideal structure underlying the ground-state charge distribution of low-density wires is made difficult by the unavoidable distortions imposed by the finite sample size and by the likely mismatch of the optimal lattice parameter with the other length scales entering the definition of our model, such as the background radius and the wire length. However, the major difficulty in characterizing the particles' geometry arises from a variety of point and extended defects such as dislocations and grain boundaries that are distributed in the structures produced by our energy optimization (see Fig. 10) both for the $N=480$ [Fig. 10(a)] and for the $N=240$ systems [Fig. 10(b)]. These defects are likely to result, at least to some extent, from limitations of our computational scheme, unable to reach the absolute minimum of the density-functional energy within an acceptable number of iterations. More importantly, the disorder in the electron droplets distribution certainly reflect a real and relevant property of these low energy systems, having a vast number of similar but different configurations of nearly equal energy. In turn, the positional disorder frozen into low energy configurations is likely to affect the properties of electron density systems measured in experiments and to give rise to glasslike features in the thermodynamics and real-time dynamics of low density wires.

Despite the unavoidable uncertainties due to the intrinsic disorder of the structures resulting from our computations, information on the underlying ground state structure can be obtained from average quantities such as the radial distribution function $g(r)$ and the coordination number n_c, defined as the value of the running coordination number up to a distance corresponding to the first minimum of the radial distribution function ($r_{\min}=2.3r_s$ for wires of $r_s \geq 50$). The similarity of the particles' $g(r)$ with those of the OCP already pointed out above clearly suggests a close relation with a bcc lattice. The coordination number n_c of the charge blobs residing in the inner shell of the computed structures is close to but nevertheless systematically lower than the $n_c=14$ value that corresponds to the number of first and second neighbors in the bcc structure (see Fig. 9). However, the absence of the shell closing at $n_c=8$, also expected for bcc, once again prevents a fully unambiguous identification. A detailed analysis of the structures found for the $N=240$ and $N=480$ samples however suggest that it might be more appropriate to characterize the computed geometries as being intermediate between fcc and bcc lattices.[50]

At the highest r_s's considered in our study ($r_s \geq 70$), the separation of the density peaks is so marked that it is pos-

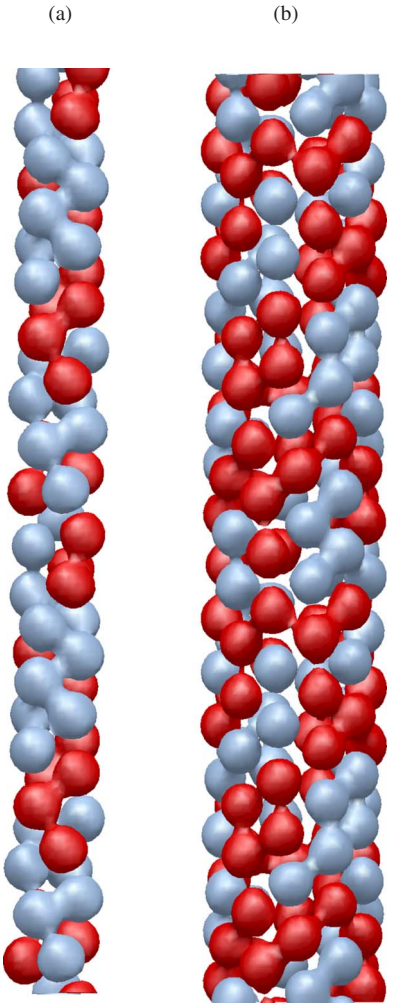

FIG. 11. (Color online) Spin polarization of charge droplets for the $r_s=70$, $\zeta=0$ wire. Red: spin up droplets. Blue: spin down droplets. The (a) inner and (b) outer shells are shown separately.

sible and even easy to identify the spatial domain occupied by each blob. This allows us to verify that not only the number of droplets corresponds to the number N of electrons, but, in addition, the integral of the charge density for each blob is very close to 1, the standard deviation amounting to only 5%. At low density, therefore, blobs can be identified with electrons, even though they should not be identified with KS orbitals, as will be discussed later. The remarkable correspondence of density blobs and electrons arises from well known anomalies in the response functions, which in reciprocal space identify the Brillouin zone of the Wigner crystal, and in real space delimit the lattice unit cell, thus determining the size, charge, and spin of the basic building block.

Individual charge blobs always display partial (at $r_s<70$) or full ($r_s\geq 70$) spin polarization for all systems in which localization is apparent, irrespective of the average polarization ζ and including nominally paramagnetic samples. Needless to say, this implies that the electronic structure of low-ζ systems includes a spin-compensating mechanism, such as antiferromagnetic ordering or a more general spin wave, bringing the net spin to the value imposed by the N_+ and N_-

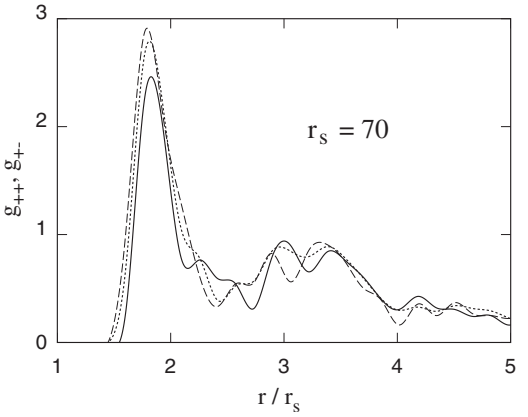

FIG. 12. Spin-resolved radial distribution function of particles representing charge blobs for a wire of size $N=240$ at $r_s=70$, $\zeta=0$. Full line: parallel spins and dash line: antiparallel spins. The radial distribution function of the corresponding system at $\zeta=1$ is shown for comparison (dotted line).

values. This is apparent in Fig. 11, displaying the spin polarization of charge blobs for the wire $r_s=70$, $\zeta=0$ wire. The spin configuration of the outermost shell is fairly disordered, while the inner shell displays a regular helical pattern [not very clear in Fig. 11, as in any two-dimensional (2D) representation but apparent in computer visualizations that allow one to rotate the isosurface] probably related to the enhancement of the spin-spin response function at $k_z=2K_F$ and $k_z=4K_F$.[51]

The disordered spin distribution of the outer shell suggests that the spin-spin coupling constant is fairly small, as confirmed by the computation of the spin-resolved radial distribution functions $g_{++}(r)$ and $g_{+-}(r)$ (see Fig. 12), which show only a slight predominance of antiferromagnetic coupling in the first coordination shell. This could be seen as the expected consequence of a nearly disjoint charge and spin blobs, reducing also the exchange interaction. It is important to realize, however, that localization concerns the density, not necessarily the KS orbitals. We verified, in fact, that even

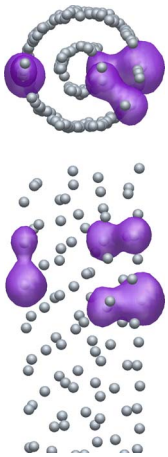

FIG. 13. (Color online) Density isosurface $\rho_1=0.05\rho_b$ for a KS orbital whose eigenvalue is close to the top of the occupied band. $r_s=70$, $N=240$ fully spin polarized ground state. The solid particles mark the center of mass position of individual charge blobs.

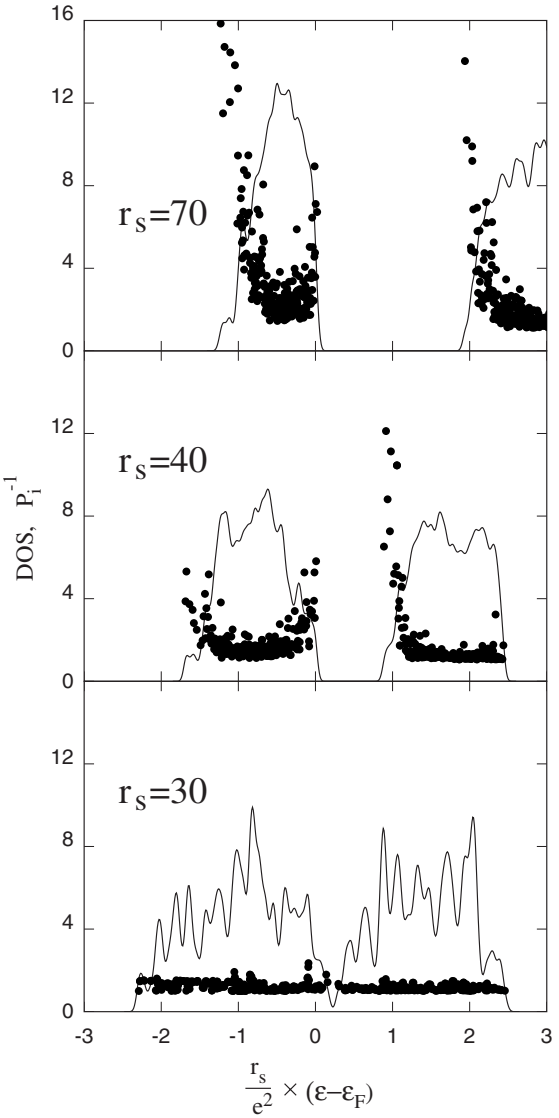

FIG. 14. Density of states and inverse participation ratio p_i^{-1} for the fully spin polarized wires at $r_s=30$, 40 and 70, $N=240$

in samples displaying the most apparent charge localization, each KS orbital contributes to the density of several, widely spaced blobs, as can be seen in Fig. 13. The qualitative information contained in this figure is confirmed by a quantitative measure of localization provided by the computation of the inverse participation ratio, which, apart from a few cases, points to a remarkably low localization for KS orbitals, as discussed below.

Charge and spin localization are nevertheless clearly reflected into basic properties of the KS orbitals, affecting, for instance, the system DOS. As can be seen in Fig. 14, the density of states for the $r_s=30$, $\zeta=1$ sample shows a deep minimum (pseudogap) at the Fermi energy, pointing to an incipient metal-insulator transition driven by localization. The $r_s=40$, $\zeta=1$ sample is clearly an insulator, and at $r_s=70$, $\zeta=1$ the energy gap separating occupied and unoccupied states is as wide as the total width of the occupied bands.

The localization of individual orbitals is measured by computing the inverse participation ratio, defined as follows.

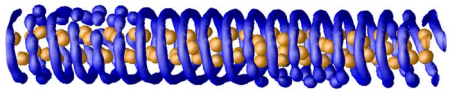

FIG. 15. (Color online) Density isosurface $\rho=2\rho_b$ for the sample of $N=240$ electrons, $r_s=100$, $\zeta=0$.

First of all, we compute the z-dependent planar average of each orbital defined as

$$\psi_i^{\text{plane}}(z) = \frac{\int \psi_i(x,y,z)dxdy}{\pi R_c^2}, \tag{14}$$

then the inverse participation ratio p_i^{-1} is computed according to

$$p_i^{-1} = L\frac{\int |\psi_i^{\text{plane}}(z)|^4 dz}{[\int |\psi_i^{\text{plane}}(z)|^2 dz]^2}. \tag{15}$$

The definition implies that localized states correspond to $p^{-1}\sim L$ and delocalized states to $p^{-1}\sim 1$. The results, reported in Fig. 14, show that the central and major portions of the occupied band is made of fairly delocalized states, while the most localized orbitals are found at the low- and high-energy band edges. While the localization of these states could have been expected, the relative delocalization of all the other states is more surprising, given the apparent strong localization of the charge.

The different behavior of the density and of KS orbitals with respect to localization might be related to the invariance of LSD with respect to unitary transformation of the occupied states, which, by definition, leave the electron density and the kinetic energy unchanged. A better correspondence of charge blobs and KS orbitals at $r_s>40$ could possibly emerge from a Wannier function representation of the electronic structure, which, however, requires a less elementary account of k_z-point sampling as well as more demanding computations.

We verified that the DOS and localization properties illustrated here by results for samples of $N=240$ electrons are the same as those of the larger samples with $N=480$ electrons, suggesting that they are more related to basic electron gas (and jellium) properties than to the details of inhomogeneity and confinement in the wire geometry. On the other hand, all the effects described in this section are likely to affect the transport properties of nearly 1D low-carrier density conductors. As a last observation, we would like to mention that at the lowest densities explored by our computations ($80\leq r_s \leq 100$) the plane-wave energy optimization gives rise to surprising new structures, especially for the low spin samples, as shown in Fig. 15 for the $N=240$ wire of $r_s=100$, $\zeta=1$.

IV. DISCUSSION AND CONCLUSIVE REMARKS

A jellium model of conducting wires has been investigated by DF-LSD computations spanning a wide range of

densities ($1 \leq r_s \leq 100$) and spin polarizations ($0 \leq \zeta \leq 1$). A computational scheme free of shape approximations and symmetry restrictions has been adopted based on a plane wave expansion for the Kohn–Sham orbitals. The model explicitly describes a fairly large number of electrons ($N=240$ and $N=480$) on a finite wire segment periodically repeated in space to approach a continuous extended wire. The actual diameter and length of the wire are proportional to r_s, reaching the mesoscopic range at low density (high r_s). The plane-wave convergence has been tested by comparison with a cylindrically symmetric computation at low r_s.

Starting from a paramagnetic ground state, spin polarization arises at $r_s \sim 30$, in qualitative agreement with previous studies using a 1D model with an effective electron-electron potential and an *ad hoc* XC approximation.[31] The transition to a spin polarized state is accompanied by an apparent change in the density, displaying a strong enhancement of the radial oscillations, as well as a marked modulation in the z direction. Close to the transition point the spin polarization is only partial ($\zeta \sim 0.5$), and also the electron localization is incomplete, giving rise to a density and spin distribution reminiscent of the broken symmetry state found by LSD computations for the homogeneous electron gas at comparable background densities. The absolute value of the spin polarization energy is very small on both sides of the transition point, and the transition itself is at most only weakly first order. Both spontaneous spin polarization and electron localization seen in our computations have a counterpart in the results of recent experiments.[24–26]

Our unconstrained computations offer a wealth of information on the ground state structure of the broken symmetry phase. At sufficiently low density ($r_s \geq 40$) electron localization is complete, and the ground state is a collection of charge droplets, each corresponding to one electron and $1/2\mu_B$. The broken symmetry state is an insulator, and therefore the transition could be detected by measurements of the low frequency electric conductivity. Other general spectroscopic properties such as the Raman spectrum might also be significantly affected by the transition that is likely to change also the frequency, strength, and dispersion relation of plasmon excitations.

The distribution of the charge droplets is fairly regular and defines a lattice whose structure is intermediate between bcc and fcc. Nevertheless, several defects are distributed in the lowest-energy structures found by our numerical minimization. Disorder is apparent also in the spin distribution, which shows only a weak preference for antiferromagnetic coupling. Both positional and spin disorders might give rise to glasslike features in the conductivity and in the Raman excitation spectrum of low-density wires.

Charge localization into one-electron droplets does not identically correspond to localization of the Kohn–Sham orbitals. Nevertheless, the paramagnetic transition and the successive progressive localization are clearly reflected in the DOS and in the inverse participation ratio of electron states. As shown in Fig. 14, at all densities the central portion of the valence band is made of delocalized KS orbitals. At $r_s > 30$, however, the high- and low-energy tails of the band display increasing localization with decreasing background density. Quasilocalized states at the band edge are likely to be very sensitive to even small perturbations in the external potential[52] due, for instance, to lattice defects or to fluctuations in the doping concentration. At densities close to the magnetic and localization transition, therefore, the combination of quasilocalized states and potential fluctuations might greatly affect the wire conductivity and its spin polarization. In this respect, and despite the different dimensionality, the picture emerging from the present study appears to be closely related to the results of recent experiments,[53,54] pointing to spontaneous spin polarization and localization in 2D electron systems in high-mobility GaAs/AlGaAs heterostructures.

The application of LSD to a quasi-1D system is justified by the fairly large diameter of the wires considered in the present study, and by the fact that several subbands are populated in the ground-state configuration. On the other hand, the application of a mean-field approximation such as LSD to the highly correlated low-density regime is not without drawbacks. Additional problems might arise from spin contamination.

The LSD prediction of partial spin polarization and partial density localization in the heg at densities as high as $r_s=22$ has been seen as a clear indication that LSD fails in the low-density high correlation regime since fixed-nodes diffusion QMC computations provide a fairly different picture of the heg phase diagram, predicting a first transition from the paramagnetic state to a partially spin polarized, but still homogeneous fluid at $r_s=25$ and a second transition to a Wigner crystal at $[(65 \pm 10) \leq r_s < 106]$.[36,40,41] However, even in the case of the heg the comparison still leaves a narrow margin of uncertainty since QMC computations have been performed only under rather restrictive choices for the nodal surface of the ground state wave function. The uncertainty is larger in the case of the wire, whose density is already nonuniform at all r_s values. Further investigations of this issue would be highly desirable.

Spin contamination is likely to be present in our unrestricted solutions, in which we easily select the S_z component of the spin, but cannot determine the spin length S. However, spin contamination has often been found to be less severe in LSD than in other approximations relying on the exact exchange.[55]

By considering the appropriate limit of the relativistic Dirac equations, we verified that the spin-orbit energy arising from the jellium background is negligible. In real systems, however, spin-orbit interactions with the underlying atoms might be important and might affect the energy ordering of subbands.[56] This, in turn, might modify the quantitative details of the picture provided by our computations, but the qualitative features are likely to remain the same. On the other hand, noncollinear spin states, excluded by our simple LSD scheme, might instead appear as broken symmetry solutions both in real systems and in more sophisticated determinations of the nanowire electronic structure. In this respect, the complex density distribution found by our energy minimization at $r_s=100$, $\zeta=0$ provides clear evidence that intriguing surprises may still be expected even from the simplest jellium model of nanowires.

[1] *Nanotechnology Research Directions: Vision for Nanotechnology Research and Development in the Next Decade*, edited by M. C. Roco, S. Williams, and P. Alivisatos (Springer, Heidelberg, 2000); P. Moriarty, Rep. Prog. Phys. **64**, 297 (2001).
[2] R. S. Friedman, M. C. McAlpine, D. S. Ricketts, D. Ham, and C. M. Lieber, Nature (London) **434**, 1085 (2005).
[3] B. J. van Wees, H. van Houten, C. W. J. Beenakker, J. G. Williamson, L. P. Kouwenhoven, D. van der Marel, and C. T. Foxon, Phys. Rev. Lett. **60**, 848 (1988); D. A. Wharam, T. J. Thornton, R. Newbury, M. Pepper, H. Ahmed, J. E. F. Frost, D. G. Hasko, D. C. Peacock, D. A. Ritchie, and G. A. C. Jones, J. Phys. C **21**, L209 (1988).
[4] C. Yannouleas and U. Landman, J. Phys. Chem. B **101**, 5780 (1997); C. Yannouleas, E. N. Bogachek, and U. Landman, Phys. Rev. B **57**, 4872 (1998).
[5] L. Kuipers and J. W. M. Frenken, Phys. Rev. Lett. **70**, 3907 (1993); G. Rubio, N. Agraït, and S. Vieira, *ibid.* **76**, 2302 (1996).
[6] J. M. Krans, J. M. van Ruitenbeek, V. V. Fisun, I. K. Yanson, and L. J. de Jongh, Nature (London) **375**, 767 (1995); A. I. Yanson, I. K. Yanson, and J. M. van Ruitenbeek, Phys. Rev. Lett. **87**, 216805 (2001).
[7] N. W. Gong, M. Y. Lu, C. Y. Wang, Y. Chen, and L. J. Chen, Appl. Phys. Lett. **92**, 073101 (2008); S. H. Kim, W. I. Choi, G. Kim, Y. J. Song, G.-H. Jeong, R. Hatakeyama, J. Ihm, and Y. Kuk, Phys. Rev. Lett. **99**, 256407 (2007); C. T. White and T. N. Todorov, Nature (London) **393**, 240 (1998).
[8] W. S. Yun, J. Kim, K. H. Park, J. S. Ha, Y. J. Ko, K. Park, S. K. Kim, Y. J. Doh, H. J. Lee, J. P. Salvetat, and L. Forro, J. Vac. Sci. Technol. A **18**, 1329 (2000).
[9] M. Endo, M. S. Strano, and P. M. Ajayan, in *Carbon Nanotubes*, Topics in Applied Physics Vol. 111 (Springer-Verlag, Berlin, 2008), pp. 13–61.
[10] A. R. Goñi, A. Pinczuk, J. S. Weiner, J. M. Calleja, B. S. Dennis, L. N. Pfeiffer, and K. W. West, Phys. Rev. Lett. **67**, 3298 (1991).
[11] A. Schmeller, A. R. Goni, A. Pinczuk, J. S. Weiner, J. M. Calleja, B. S. Dennis, L. N. Pfeiffer, and K. W. West, Phys. Rev. B **49**, 14778 (1994); C. Schüller, G. Biese, K. Keller, C. Steinebach, D. Heitmann, P. Grambow, and K. Eberl, *ibid.* **54**, R17304 (1996); Z. Zanolli, M.-E. Pistol, L. E. Fröberg, and L. Samuelson, J. Phys.: Condens. Matter **19**, 295219 (2007).
[12] The interaction of charge carriers with the underlying semiconductor material still determines parameters such as the effective mass and the dielectric constant.
[13] T. A. Skotheim, R. L. Elsenbaumer, and J. Reynolds, *Handbook of Conducting Polymers* (Dekker, New York, 1998).
[14] See, e.g., T. Giamarchi, *Quantum Physics in One Dimension* (Clarendon, Oxford, 2004).
[15] G. F. Giuliani and G. Vignale, *Quantum Theory of the Electron Liquid* (Cambridge University Press, Cambridge, England, 2005).
[16] D. Pines and Ph. Noziere, *The Theory of Quantum Liquids* (Benjamin, New York, 1966).
[17] J. M. Luttinger, J. Math. Phys. **4**, 1154 (1963); S. Tomonaga, Prog. Theor. Phys. **5**, 544 (1950); M. P. A. Fisher and A. Glazman, *Mesoscopic Electron Transport* (Kluwer, Boston, 1997).
[18] S. V. Zaitsev-Zotov, Y. A. Kumzerov, Y. A. Firsov, and P. Monceau, J. Phys.: Condens. Matter **12**, L303 (2000).
[19] M. Bockrath, D. H. Cobden, J. Lu, A. G. Rinzler, R. E. Smalley, L. Balents, and P. L. McEuen, Nature (London) **397**, 598 (1999); Z. Yao, H. W. C. Postma, L. Balents, and C. Dekker, *ibid.* **402**, 273 (1999); A. Bachtold, M. de Jonge, K. Grove-Rasmussen, P. L. McEuen, M. Buitelaar, and C. Schonenberger, Phys. Rev. Lett. **87**, 166801 (2001).
[20] P. Horsch, M. Sofin, M. Mayr, and M. Jansen, Phys. Rev. Lett. **94**, 076403 (2005); K. Hiraki and K. Kanoda, *ibid.* **80**, 4737 (1998).
[21] S. Biermann, A. Georges, T. Giamarchi, and A. Lichtenstein, in *Strongly Correlated Fermions and Bosons in Low-Dimensional Disordered Systems*, edited by I. V. Lerner, B. L. Altshuler, V. I. Fal'ko, and T. Giamarchi (Kluwer, Amsterdam, 2002), p. 81.
[22] Early reports of Luttinger behavior might have been influenced by the marked modulation of the wire cross section at metal point contacts.
[23] H. J. Schulz, Phys. Rev. Lett. **71**, 1864 (1993).
[24] A. Rahman and M. K. Sanyal, Phys. Rev. B **76**, 045110 (2007).
[25] V. V. Deshpande and M. Bockrath, Nat. Phys. **4**, 314 (2008).
[26] R. Danneau, O. Klochan, W. R. Clarke, L. H. Ho, A. P. Micolich, M. Y. Simmons, A. R. Hamilton, M. Pepper, and D. A. Ritchie, Phys. Rev. Lett. **100**, 016403 (2008); K. J. Thomas, J. T. Nicholls, M. Y. Simmons, M. Pepper, D. R. Mace, and D. A. Ritchie, *ibid.* **77**, 135 (1996); R. D. Tscheuschner and A. D. Wieck, Superlattices Microstruct. **20**, 615 (1996).
[27] A. Gold and L. Calmels, Philos. Mag. Lett. **74**, 33 (1996).
[28] C. A. Stafford, D. Baeriswyl, and J. Bürki, Phys. Rev. Lett. **79**, 2863 (1997); J. M. van Ruitenbeek, M. H. Devoret, D. Esteve, and C. Urbina, Phys. Rev. B **56**, 12566 (1997); N. Zabala, M. J. Puska, and R. M. Nieminen, *ibid.* **59**, 12652 (1999).
[29] N. Zabala, M. J. Puska, and R. M. Nieminen, Phys. Rev. Lett. **80**, 3336 (1998).
[30] K. Kärkkäinen, M. Koskinen, S. M. Reimann, and M. Manninen, Phys. Rev. B **72**, 165324 (2005); S. M. Reimann, M. Koskinen, and M. Manninen, *ibid.* **59**, 1613 (1999).
[31] B. Tanatar, I. Al-Hayek, and M. Tomak, Phys. Rev. B **58**, 9886 (1998).
[32] M. Casula, S. Sorella, and G. Senatore, Phys. Rev. B **74**, 245427 (2006); M. Casula and G. Senatore, ChemPhysChem **6**, 1902 (2005).
[33] J. Rech and K. A. Matveev, Phys. Rev. Lett. **100**, 066407 (2008); M. M. Fogler and E. Pivovarov, Phys. Rev. B **72**, 195344 (2005); E. J. Mueller, *ibid.* **72**, 075322 (2005).
[34] N. W. Ashcroft and N. D. Mermin, *Solid State Physics* (Holt, London/Saunders, Philadelphia, 1976).
[35] W. A. de Heer, Rev. Mod. Phys. **65**, 611 (1993); M. Brack, *ibid.* **65**, 677 (1993).
[36] D. M. Ceperley and B. J. Alder, Phys. Rev. Lett. **45**, 566 (1980).
[37] F. Sottile and P. Ballone, Phys. Rev. B **64**, 045105 (2001).
[38] J. P. Perdew, K. Burke, and M. Ernzerhof, Phys. Rev. Lett. **77**, 3865 (1996).
[39] G. Senatore and G. Pastore, Phys. Rev. Lett. **64**, 303 (1990).
[40] G. Ortiz, M. Harris, and P. Ballone, Phys. Rev. Lett. **82**, 5317 (1999).
[41] See, N. D. Drummond, Z. Radnai, J. R. Trail, M. D. Towler, and R. J. Needs, Phys. Rev. B **69**, 085116 (2004).
[42] J. P. Perdew and A. Zunger, Phys. Rev. B **23**, 5048 (1981).
[43] See, however, further remarks on this comparison in Sec. III B.
[44] The expression *cylindrical symmetry* is used to denote both rotational symmetry (C_∞) around a fixed axis and translational invariance along the axis' direction.

[45] D. Marx and J. Hutter, in *Modern Methods and Algorithms of Quantum Chemistry*, NIC Series Vol. 1, edited by J. Grotendorst (John von Neumann Institute for Computing, Jülich, 2000), pp. 301–449.

[46] The Fermi wave vector of spin-up and spin-down electrons in an homogeneous electron gas of spin polarization ζ are given by (a.u.): $K_{F\uparrow}=1/r_s(9\pi/4(1+\zeta))^{1/3}$ and $K_{F\downarrow}=1/r_s(9\pi/4(1-\zeta))^{1/3}$, and the corresponding kinetic energy per electron is $KE=3/10(K_{F\uparrow}^5+K_{F\downarrow}^5/K_{F\uparrow}^3+K_{F\downarrow}^3)$.

[47] A. V. Filinov, M. Bonitz, and Yu. E. Lozovik, Phys. Rev. Lett. **86**, 3851 (2001).

[48] It is important to note that the radial distribution functions and the running coordination number discussed in the present paper on the basis of a particle representation of the continuous electron density is not the same electron-electron radial distribution function computed in previous QMC studies (see Refs. 40 and 41), even though the two definitions become progressively similar with increasing electron localization.

[49] S. Tanaka and S. Ichimaru, Phys. Rev. A **35**, 4743 (1987).

[50] The bcc and fcc lattices are related by a continuous transformation (Bain's path).

[51] J. P. Pouget and S. Ravy, Synth. Met. **85**, 1523 (1997).

[52] M. Evaldsson, S. Ihnatsenka, and I. V. Zozoulenko, Phys. Rev. B **77**, 165306 (2008).

[53] C. Siegert, A. Ghosh, M. Pepper, I. Farrer, and D. A. Ritchie, Nat. Phys. **3**, 315 (2007).

[54] A. Ghosh, C. J. B. Ford, M. Pepper, H. E. Beere, and D. A. Ritchie, Phys. Rev. Lett. **92**, 116601 (2004).

[55] See, for instance, D. Harris and G. H. Loew, J. Am. Chem. Soc. **101**, 3959 (1997).

[56] F. Malet, M. Pi, M. Barranco, L. Serra, and E. Lipparini, Phys. Rev. B **76**, 115306 (2007).